PRE-PRINT: I. El Mokhtar, L. Gurreri, A. Tamburini, A. Cipollina, M. Ciofalo, S. al T. Bouguecha, G. Micale, *CFD prediction of flow, heat and mass transfer in woven spacer-filled channels for membrane processes*, Int. J. Heat Mass Transf. 173 (2021) 121246, https://doi.org/10.1016/j.ijheatmasstransfer.2021.121246

CFD prediction of flow, heat and mass transfer in woven spacer-filled channels for membrane processes

Imen El Mokhtar[1], Luigi Gurreri[2*], Alessandro Tamburini[2], Andrea Cipollina[2], Michele Ciofalo[2], Salah al Taher Bouguecha[3], Giorgio Micale[2]

1 Water, membrane and environmental biotechnology laboratory, Water Researches and Technologies Center, Borj-Cedria Technopark, Tourist Route of Soliman-Nabeul, 8020 Soliman, Tunisia

2 Dipartimento di Ingegneria, Università degli Studi di Palermo, Viale delle Scienze ed. 6, 90128 Palermo, Italy

3 Department of Mechanical Engineering, Faculty of Engineering, King Abdul-Aziz University, P.B: 80204 Jeddah 21589, Saudi Arabia

**Corresponding author: luigi.gurreri@unipa.it*

Abstract

Flow and heat or mass transfer in channels provided with woven spacers made up of mutually orthogonal filaments were studied by Computational Fluid Dynamics. The problem addressed was the combined effect of the parameters that characterize the process: pitch to height ratio P/H (2, 3 and 4), flow attack angle θ (0, 7, 15, 20, 30, 40 and 45°) and Reynolds number Re (from ~1 to ~4000). The Prandtl number was 4.33, representative of water at ~40 °C, while the Schmidt number was 600, representative of NaCl solutions. Simulations were performed by the finite volume code Ansys CFX™ 18.1 using very fine grids of ~6 to ~14 million volumes. For Re>3-400, the SST turbulence model was used to predict flow and heat transfer; no simulations of mass transfer were performed in the turbulent regime because the resolution of the diffusive sublayer would have required a prohibitive number of grid points. Results were validated against experimental data, including results obtained by Liquid Crystal Thermography and Digital Image Processing. The flow attack angle θ=45° was the most effective for mixing (higher Nusselt number, Nu, and Sherwood number, Sh) and caused lower values of friction coefficient (f). In the range investigated, increasing the pitch to height ratio P/H caused Nu, Sh and f all to decrease. Therefore, the highest values of Sh and Nu were provided by the configuration P/H=2, θ=45°. Compared with non-woven spacers, woven spacers provided a better mixing, especially at intermediate values of Re, but at the expenses of higher pressure drops.

Keywords: Woven spacer; Pressure drop; Concentration polarization; Temperature polarization; Computational Fluid Dynamics; SST turbulence model.

1. Introduction

1.1 Performance characteristics of membrane processes

As the need for freshwater becomes an issue of more and more vital importance, desalination technologies, and especially membrane separation processes, are developing rapidly. Current progresses in the desalination industry have been related to the fast growth of membrane technology, the design and creation of new materials that enhance the specific productivity and selectivity, as well the manufacturing of optimized membrane stack geometries in order to reach various objectives, such as compactness, lower pressure losses and durability.

In parallel with the rapid development of membrane technology, there has been also a growing interest in the understanding of the fluid dynamics and of the complex influence of spacers.

In pressure-driven membrane processes [1,2], spacers increase mass transfer rates by reducing the thickness of concentration boundary layers and enhancing mixing in the direction perpendicular to the mean flow; examples can be found in Reverse Osmosis, or RO [3], and Ultra-Filtration, or UF [4]. Likewise, in thermally-driven processes such as membrane Distillation, or MD [5–7], spacers increase heat transfer rates by reducing the thickness of temperature boundary layers.

Unfortunately, the prices for the use of channel spacers in membrane process are the reduction of the active membrane area due to so called “shadow effects” and the increase of the pressure loss along the channel [8]. In particular, this latter quantity directly affects pumping power and thus energy consumption in all membrane processes. In addition, in processes where the driving force is a trans-membrane pressure gradient, such as the above mentioned RO and UF, pressure drop reduces the driving force available for separation. Finally, in thermally driven processes, such as MD, pressure

drop affects pressure levels in the channels, which may lead to membrane flooding and to structural problems.

Therefore, a good design of spacers as mixing promoters is crucial in all membrane processes, including either flat sheet or spiral wound modules.

1.2 Literature review

A number of experimental and computational studies have been presented in the literature on fluid flow and heat or mass transfer in spacer-filled channels for membrane processes. Here, only some recent work concerning *woven* spacers will be reviewed.

On the experimental side, Li *et al.* [9] tested two commercially available woven spacers, finding that their mass transfer / pressure drop properties were sub-optimal. Liu *et al.* [10] carried out experiments on mass transfer and pressure drop in UF with static mixer spacers, showing a performance comparable with that of conventional woven spacers. Hagedorn *et al.* [11] tested various commercial spacers, including two woven spacers, in MD experiments. Since the various spacer shapes (diamond, asymmetrical and woven) had different thickness and mesh size, the results obtained cannot be easily compared nor generalized.

More complex geometries represented by woven "tricot" mesh spacers [12] can be regarded as an evolution of simpler configurations with two layers. Pressure retarded osmosis exhibited enhanced performance with a woven spacer embedded in the support layer of the membrane, together with a "tricot" fabric spacer in the feed channel [13]. Gurreri *et al.* [14] obtained experimental values of pressure drop in ED or RED stacks and compared them with CFD predictions. Ponzio *et al.* [15] used Thermochromic Liquid Crystal sheets and Digital Image Processing to measure heat transfer coefficient distributions in plane channels filled with woven spacers of P/H=2, purposely built at 3:1 scale with respect to commercial MD applications and subjected to heat transfer from one side.

On the computational side, Gurreri *et al.* [16] first performed finite-volume CFD simulations to predict flow and mass transfer within woven spacer-filled channels, focusing on low Reynolds

numbers typical of Electrodialysis or Reverse Electrodialysis. A Neumann boundary condition (uniform mass flux) was applied for the solute concentration at the walls representing the membrane interface. A subsequent parametrical study by the same authors [8] for pitch-to-height ratio P/H=2, 3, 4, flow attack angle θ=0, 45°, orthogonal filaments, Re=1-64 showed that woven spacers outperform non-woven spacers (made by two overlapped layers). Literature data were used for model validation in that work, and then original experimental data were collected [14], finding a good agreement in both cases. Ponzio *et al.* [15] studied via CFD flow and heat transfer in a woven spacer for membrane distillation at P/H=2, θ=0 or 45°, Re=2-2000, finding a good agreement with their own experimental data. Unsteadiness and transition to turbulence were also studied for the same geometry by time-dependent direct numerical simulation [17]. In comparison with the corresponding non-woven spacers, the woven ones exhibited better mixing at the investigated flow attack angles of 0 and 45° [18].

Further CFD studies on woven spacers for membrane processes include pressure drop predictions by Johannink *et al.* [19] for $P/H\approx$2-16, θ=0 or 45° and Re up to ~1000. A sensitivity analysis of pressure drop on design parameters of woven and non-woven spacers was performed by CFD simulations in order to build a predictive model. The simulation tool was developed by the Lattice Boltzmann method. A cluster with 512-2048 processors was used. The computational domain was a sequence of several periodic cells with inlet-outlet boundary conditions. The parameters that were allowed to vary were the filaments diameter, the filaments pitch, and, in the only case of non-woven spacers, the angle between the filaments. This was, instead, fixed at 90° for woven spacers. Simulation results for a woven spacer were validated against experimental data collected either with an ED stack or with a single spacer-filled channel (in this case, the flow attack angle was 0), finding a satisfactory agreement. Simulation results were presented as iso-lines of friction coefficient as a function of different couples of parameters, including the fluid velocity. The friction factor was reported to be more sensitive to the velocity and the filaments diameter than to the other geometrical features. As in all the other studies, the pressure drop was higher in the woven configurations.

Flow and mass transfer were predicted by Gu *et al.* [20] in 2-layer non-woven, partially woven, middle (i.e. floating) layer and woven spacers for RO applications at P/H=4.5, Re=224, intrinsic angle between the filaments of 30, 60 or 90°, and θ=30, 60 or 90°. The finite-element code COMSOL Multiphysics® was used. Inlet-outlet boundary conditions were imposed in computational domains representing a unit cell, multiple cells or even less than one unit cell (1.4–2.9 million elements). The membrane surface was simulated as permeable to water and salt. Results showed that fully woven spacers were effective in reducing concentration polarization and enhancing water flux, though requiring higher pressure drop.

CFD simulations were conducted by Dong *et al.* [21] for profiled membranes for Reverse Electrodialysis at Re varying between ~2 and 30. For comparison purposes, a woven spacer (P/H=2.89, θ=45°) was also simulated using a grid with 1.86 million volumes. The unit cell approach was adopted by imposing uniform flux boundary condition, and the Ansys CFX® software was used. The woven spacer exhibited higher Sh values, especially at higher Reynolds numbers, as well as at higher values of the power number (dimensionless pressure drop).

Toh *et al.* [22] performed CFD laminar simulations of flow and mass transfer for non-woven and woven spacers for RO applications at θ=45°, P/H=5.66, Re up to ~250 and two and three filament layers. Three unit cells were simulated by using extremely fine meshes (92-102.8 million finite volumes) with significant refinement close to the wall boundaries. The membrane surfaces were simulated as impermeable dissolving walls, i.e. with no slip condition for the fluid velocity and imposed concentration for the solute. The finite-volume code Ansys CFX® was used. Results showed that the two-layer woven spacer enhanced mixing compared to the non-woven spacer, though increasing hydraulic friction. Compared to the three-layer spacers, it provided slightly lower values of the Sherwood number in the lower range of Re investigated, but higher values of Sh for larger Re. Moreover, it was characterized by lower values of hydraulic friction in the whole range of Re.

Overall, both experimental data and CFD results highlighted that woven spacers cause higher pressure drop compared with non-woven spacers, but provide better mixing and thus less severe polarization phenomena at any value of both Re and power number. Moreover, they are generally characterized by better performances compared to more complex or alternative geometries (e.g. multi-layer spacers or profiled membranes).

Despite the encouraging results exhibited by woven spacers, the characterization of these simple conventional geometries is still fragmentary. This work makes a further step towards a thorough characterization of woven spacer-filled channels, by investigating some aspects that have not been explored so far. The complex influence of P/H (2, 3, 4), θ (whole range 0-45°), and Re (~1-4000) on flow and heat/mass transfer characteristics (f, Nu, Sh) has been evaluated by CFD for conventional 2-layer woven spacers with 90° angled filaments.

2. Model and methods

2.1 Systems under investigation

The spacers analyzed consist of woven 90° angled filaments of circular cross-section, characterized by one geometrical parameter, namely the pitch to height ratio P/H (**Figure 1**), of which three different values were simulated, i.e. 2, 3 and 4.

The filament diameter was $d=H/1.8$ as in previous works [8], with some filament interpenetration allowed for at the contact spots. For symmetry reasons, the significant range of the flow attack angle θ is from 0 (flow direction parallel to a filament array) to 45° (flow direction bisecting the angle formed by the two filaments arrays); the results for any other flow attack angle can be reconducted to those for θ=0-45° by applying appropriate symmetries. The CFD simulations ranged from creeping flow to fully turbulent conditions, covering the Reynolds number interval 1-4000 (see definition in Section 2.3).

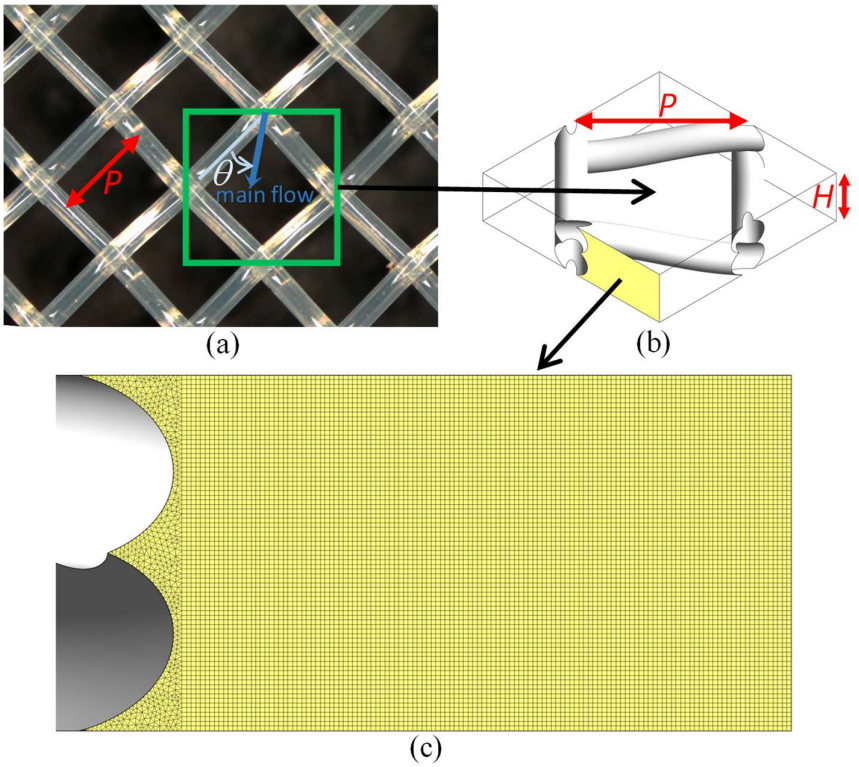

Figure 1. Spacer geometry investigated. (a) Picture of a net spacer with woven filaments; (b) Unit Cell geometry; (c) details of the mesh in the plane region highlighted in (b).

2.2 Computational domain and boundary conditions

The computational domain of the numerical simulations was built by adopting the Unit Cell approach, i.e. simulating a repetitive geometrical unit with periodic boundary conditions. This is representative of the central region of a spacer-filled channel, sufficiently far from lateral walls and inlet/outlet boundaries, where fully developed flow and concentration fields exist. The computational domain proper includes only the fluid region, excluding membranes and spacer.

Computational domains and grids were created by using Ansys Workbench™ 18.1. Because of the geometry complexity, the computational domains were discretized by hybrid grids, mainly made by hexahedra, but with tetrahedra and prisms in the regions surrounding the filaments. **Figure 1** (c) shows a detail of the computational grid. A grid independence analysis was performed by testing ten

different meshes with increasing number of volumes. For example, **Figure 2** reports the predicted values of Sh and Nu as functions of the number of finite volumes for Re_τ=80 (Re≈233), P/H=2, θ=0°.

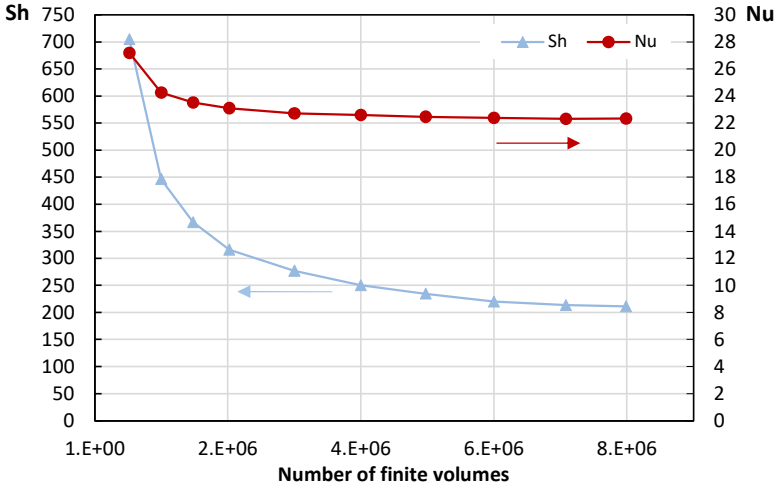

Figure 2. Values of Sh and Nu computed with ten grids for Re_τ=80 (Re≈233), P/H=2, θ=0°.

The features of the grids selected for the final simulations are reported in **Table 1**.

Table 1 Features of the meshes selected by the grid independence study.

Mesh features	***P/H*=2**	***P/H*=3**	***P/H*=4**
Number of finite volumes in height H	86	77	71
Total number of finite volumes	6,000,220	9,630,112	13,714,094
% of domain volume discretized with hexahedra	66.3	77.2	82.8

Translational periodic boundary conditions were applied at the lateral surfaces. All solid walls (fluid-spacer and fluid-membrane interfaces) were set as impermeable and with no-slip boundary conditions. Zero flux was imposed at the spacer boundary. At the top and bottom walls, representing the fluid-membrane interfaces, a Neumann condition (imposed mass flux) was set for mass transfer, and a mixed (Robin) condition for heat transfer (thermal resistance of $6.25 \cdot 10^{-3}$ K m^2 W^{-1}), as made in previous works [8,23]. For a comparison with some experimental data, thermal simulations were conducted also with one-side heat transfer, i.e. by setting one of the walls as adiabatic. In the following, if not otherwise specified, results refer to two-side heat transfer.

2.3 Governing equations, definitions and numerical details

The finite-volume code ANSYS-CFX™ 18.1 was used to discretize and solve the problem. Mathematically, the governing equations were adapted to the simulation of a periodic domain by following the "periodic unit cell" approach described in detail, for example, by Battaglia *et al*. [24]. By assuming a Newtonian, constant-property fluid and steady-state conditions, the continuity, Navier–Stokes, mass transport and energy equations describing the problem can be written in Cartesian tensor notation as follows:

$$\frac{\partial u_i}{\partial x_i} = 0 \tag{1}$$

$$\frac{\partial \rho \ _j u_i}{\partial x_j} = -\frac{\partial \tilde{p}}{\partial x_i} + \frac{\partial}{\partial x_j}\mu \frac{\partial u_i}{\partial x_j} + K_p s_i \tag{2}$$

$$\frac{\partial u_j \tilde{c}}{\partial x_j} = \frac{\partial}{\partial x_j} D \frac{\partial \tilde{c}}{\partial x_j} + K_c u_s \tag{3}$$

$$\frac{\partial \rho c_p u_j \tilde{T}}{\partial x_j} = \frac{\partial}{\partial x_j} \lambda \frac{\partial \tilde{T}}{\partial x_j} + K_T u_s \tag{4}$$

where u_i is the i-th velocity component, ρ is the density and $\tilde{p}$, $\tilde{c}$ and $\tilde{T}$ are the periodic components of pressure, concentration and temperature, respectively. $K_p=|dp/ds|$ is the pressure loss per unit length, K_c and K_T are the variations per unit length of bulk concentration c_b and enthalpy per unit volume $\rho c_p T_b$, respectively. Also, s_i is the i-th component of the unit vector **s** directed along the main flow direction; u_s = **u**·**s** is the local velocity component along the same direction; D is the solute diffusivity; c_p is the specific heat capacity; and λ is the thermal conductivity. The physical properties of the fluid corresponded to Schmidt and Prandtl numbers of 600 and 4.33, respectively.

Steady-state laminar simulations were performed up to the highest Reynolds number for which a full convergence of the solution to a stationary condition could be attained. For higher values of Re, convergence difficulties were observed: residuals remained relatively high and local values of the

variables exhibited oscillations. In these cases, the Shear Stress Transport (SST) turbulence model was employed [25]. This transition occurred for Re≈350-430, depending weakly on P/H and θ.

The SST turbulence model provides accurate solutions only if the viscous, conductive and diffusive near-wall sublayers are resolved by a sufficient number of grid points. In wall units ν/u_τ, the thickness of the viscous sublayer is $y_V^+\approx 11$ while those of the conductive and diffusive sublayers are smaller. Based on the classic experiments of Jayatilleke [26], they can be estimated to be $y_T^+\approx 8$ (Pr≈4.33) and $y_D^+\approx 1.8$ (Sc=600). The grids used in the present work (Table 1) resolve the viscous and conductive sublayers up to the highest Re investigated (~4000) but are far from resolving the much thinner diffusive sublayer. Therefore, we chose not to simulate mass transfer under turbulent flow conditions. Note that in most applications, e.g. direct and reverse electrodialysis, mass transfer in spacer-filled channels occurs under laminar flow conditions.

A different number of iterations, depending on the case simulated, were performed until all the root mean square residuals settled to values lower than 10^{-6}.

The hydraulic diameter of the void (spacerless) channel was assumed as the characteristic length:

$$d_{h,void} = 2H \tag{5}$$

Accordingly, the bulk Reynolds number was defined as [15,27]:

$$Re = \frac{U_{void}}{\nu} 2H \tag{6}$$

in which U_{void} is the average velocity in the void channel, and ν is the kinematic diffusivity. The friction velocity Reynolds number was calculated using the following expression:

$$Re_\tau = \frac{U_\tau}{\nu}\frac{H}{2} \tag{7}$$

in which $U_\tau = \sqrt{\frac{H}{2\rho}\left|\frac{dp}{ds}\right|}$ is the friction velocity. The simulations were carried out at various values of Re_τ (i.e. of pressure drop), while the flow rate and the corresponding Re were obtained as part of the solution.

The Darcy friction coefficient was computed as:

$$f = \left|\frac{dp}{ds}\right| \frac{4H}{\rho\, U_{void}^2} \tag{8}$$

With the present definitions, one has $f = 128(\mathrm{Re}_\tau/\mathrm{Re})^2$.

Mass and heat transport were characterized by Sherwood number (Sh) and Nusselt number (Nu), respectively. Local values of these dimensionless quantities were computed as:

$$Sh_{loc} = \frac{J_w''}{(c_b - c_w)} \frac{2H}{D} \tag{9}$$

$$Nu_{loc} = \frac{q_w''}{(T_b - T_w)} \frac{2H}{\lambda} \tag{10}$$

where J_w'', q_w'' are the local flux of solute and heat at the wall, respectively, c_b, T_b are the bulk (mass flow averaged) concentration and temperature, respectively, and c_w, T_w are the local wall concentration and temperature. The mean values used to characterize mass and heat transfer were calculated as [28]

$$Sh = \frac{\langle J_w'' \rangle}{(c_b - \langle c_w \rangle)} \frac{2H}{D} \tag{11}$$

$$Nu = \frac{\langle q_w'' \rangle}{(T_b - \langle T_w \rangle)} \frac{2H}{\lambda} \tag{12}$$

where $\langle J_w'' \rangle$, $\langle c_w \rangle$, $\langle q_w'' \rangle$ and $\langle T_w \rangle$ are the wall averaged values of molar flux, concentration, heat flux, and temperature, respectively.

3. Results and discussion

3.1 One-side versus two-side heat transfer

A fluid-filled plane channel can be subjected to heat transfer either on one or on both sides. In the case of Membrane Distillation (MD), one-side heat transfer is usually realized in laboratory-scale experimental rigs [15] or small-scale, plate-and-frame, MD equipment [29] because it is simpler to build and allows an easier experimental characterization of temperatures and heat fluxes. On the other hand, commercial applications of MD usually adopt two-side heat transfer since each feed channel is

sandwiched between two condensate channels [30]. As discussed in [31], the single active wall of the one-side heat transfer arrangement may exhibit a different mean heat transfer coefficient than either wall of the two-side arrangement, so that the total heat transfer is not one half.

Figure 3 compares the computed mean Nusselt number Nu as a function of the Reynolds number Re for a woven spacer with P/H=2, flow attack angle 0 or 45° and one-side or two-side heat transfer. It can be observed that the difference between one- and two-side heat transfer is large in the low Reynolds number range, while it decreases with Re and becomes negligible for Re>~400, in correspondence with the transition from laminar to turbulent flow (as defined in Section 2.3 above). Similar results are obtained for different P/H ratios and flow attack angles.

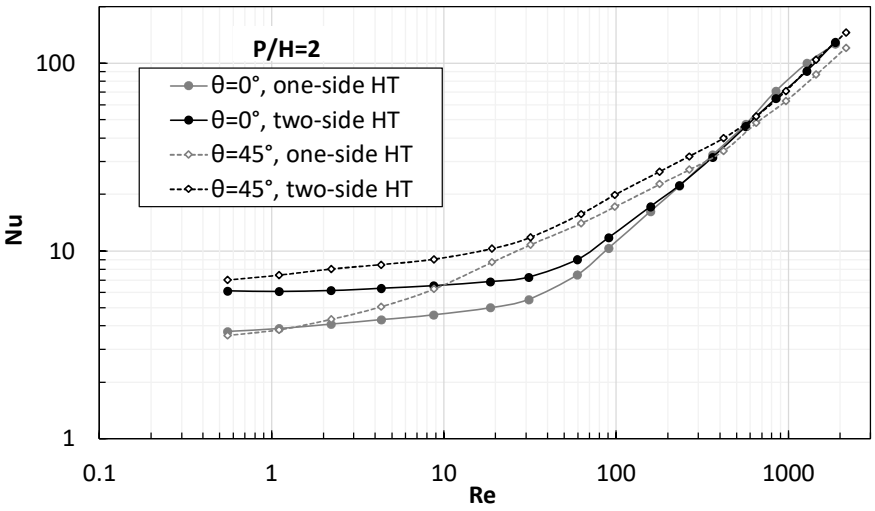

Figure 3. Nusselt number as a function of the Reynolds number for a woven spacer with P/H=2, flow attack angle 0 or 45°: comparison of CFD results for one- and two-side heat transfer.

In the following, unless otherwise specified in explicit form, results for the two-side heat or mass transfer configuration will be reported since they are more relevant to MD and other membrane processes.

3.2 Comparison with previous results

A first comparison was performed between the present results and experimental data obtained at the Department of Engineering in Palermo using different test sections simulating MD channels.

In regard to friction, **Figure 4** compares computational and experimental results for the Darcy friction coefficient f in a woven spacer with P/H=2 and a flow attack angle θ of 0° or 45°. Experimental data were obtained by pressure tappings and a piezometric pressure transducer [15]. An excellent agreement is observed for the flow attack angle of 0°, whereas experimental results are slightly underpredicted (max. 20%) for θ=45°.

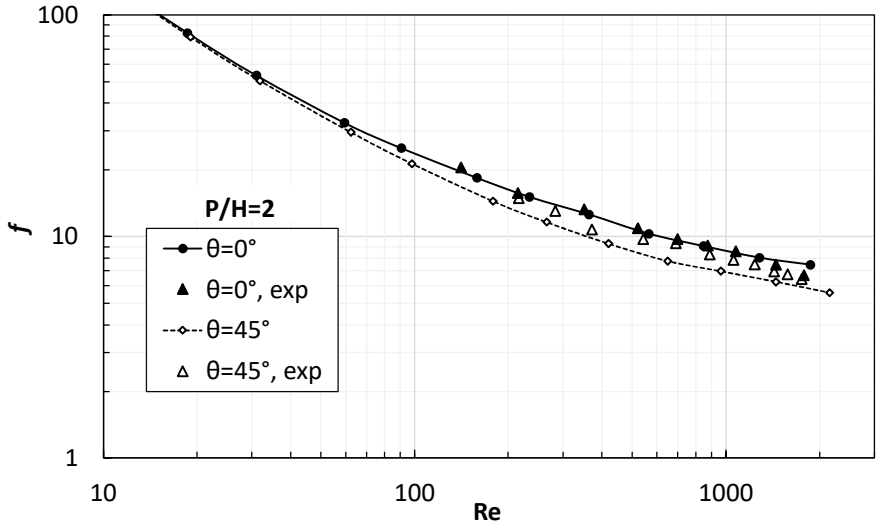

Figure 4. Darcy friction coefficient as a function of the Reynolds number for a woven spacer with P/H=2, flow attack angle 0 or 45°: comparison of computational and experimental results [15].

In regard to heat transfer, **Figure 5** compares computational and experimental results for the mean Nusselt number Nu with a woven spacer of P/H=2, flow attack angles 0° and 45° and one-side heat transfer. Experimental data were obtained by Liquid Crystal Thermography and Digital Image Processing in a test section with one-side heat transfer using the technique described in ref. [15]. The agreement is fair for both orientations.

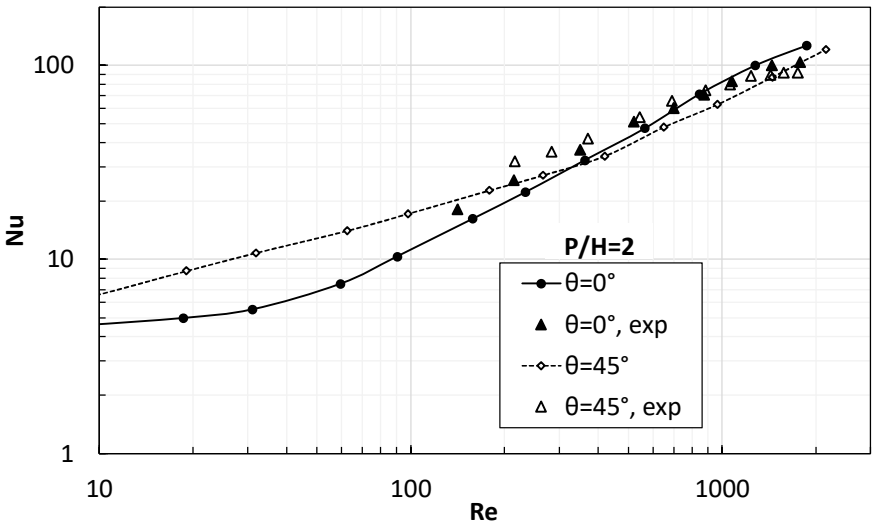

Figure 5. Nusselt number as a function of the Reynolds number for a woven spacer with P/H=2, flow attack angles of 0° and 45°, one-side heat transfer: comparison of computational results with experimental data [13].

As a further comparison, **Figure 6** reports computational and experimental results for the mean Nusselt number Nu in a woven spacer filled channel with P/H=4, flow attack angle 0° or 45° and two-side heat transfer. Experimental data were obtained by Liquid Crystal Thermography and Digital Image Processing in a test section providing two-side heat transfer [32]. Allowing for some dispersion in the experimental data, a fair overall agreement can be observed, with some discrepancy at the lower (Re≈200-300) and upper (Re≈2000-3000) ends of the range that was experimentally investigated. For Re<~200, numerical simulations predict significantly higher values of Nu for the flow attack angle θ=45° than for θ=0; unfortunately, experimental data are not available in this low-Re range.

Figure 6 reports also a single computational result (Nu=19.2) obtained by Direct Numerical Simulation (DNS) for the case θ=0, Re≈350; it is in excellent agreement both with the experimental result obtained at a very similar Re (Nu=17.8) and with the present computational results (yielding Nu≈18.4 by interpolation).

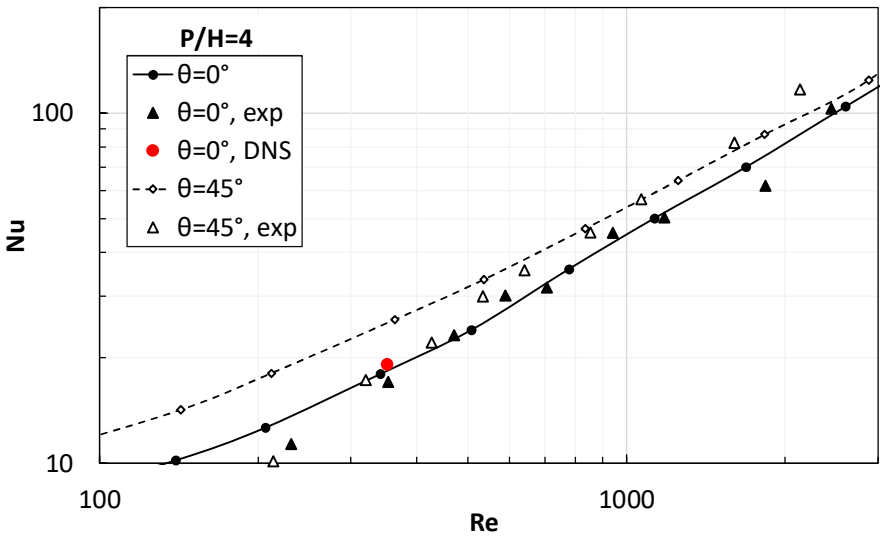

Figure 6. Nusselt number as a function of the Reynolds number for a woven spacer with P/H=4, flow attack angle 45°, two-side heat transfer: comparison of computational results with experimental data obtained by Liquid Crystal Thermography.

Figure 7 compares the present predictions for the Darcy friction coefficient, obtained at different values of P/H and flow attack angle, with literature results. These include predictions by the Lattice Boltzmann method and experimental results obtained by Johannink *et al.* [19] for P/H=1.9 and θ=0°; CFD results for P/H=2.89 and θ=45°obtained by Dong *et al.* [21] using the finite volume code Ansys CFX®; and CFD results for P/H=5.66 and θ=45° obtained by Toh *et al.* [22] using the same code and extremely fine grids of up to ~100 million volumes (three unit cells).

Taking account of the differences in P/H, the overall agreement between the present predictions and the literature results is good, especially with the LB predictions in [19].

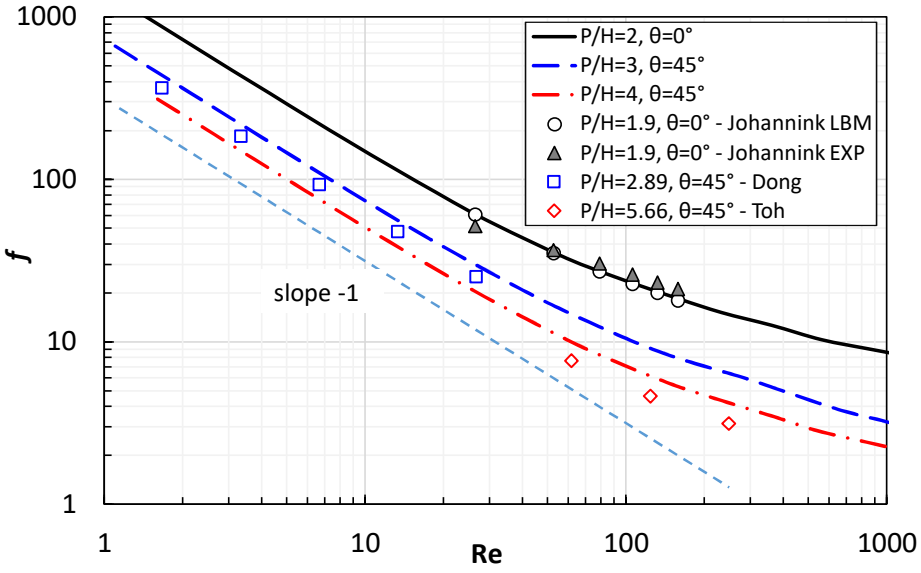

Figure 7. Darcy friction coefficient as a function of the Reynolds number for woven spacers: comparison of the present computational results with literature data by Johannink *et al*. [19], Dong *et al*. [21], Toh *et al*. [22].

Figure 8 reports a similar comparison for the Sherwood number. The literature results considered include CFD predictions obtained by Dong *et al.* [21] for P/H=2.89 and by Toh *et al.* [22] for P/H=5.66. In both studies the flow attack angle was θ=45°, the code used was Ansys CFX®; and the Schmidt number was ~600 as in the present work.

Taking again account of the different values of P/H, the agreement between the present predictions and the literature results for Sh is less satisfactory than for f, the largest discrepancy between the cases P/H=2.89 [21] and P/H=3 (present) being obtained for Re≈27.

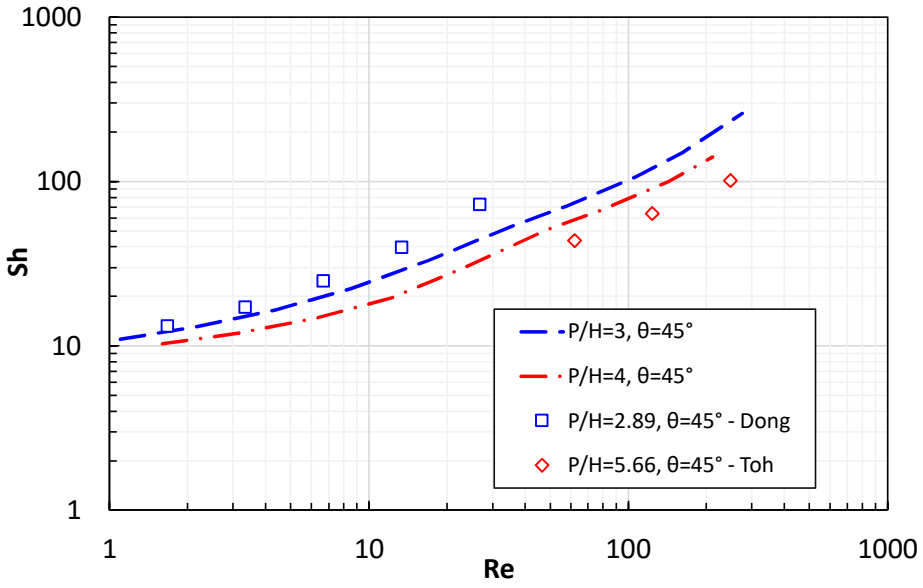

Figure 8. Sherwood number as a function of the Reynolds number for woven spacers: comparison of the present computational results with literature data by Dong *et al*. [21], Toh *et al*. [22].

3.3 Effect of the flow attack angle

Concerning the influence of the flow attack angle on the heat/mass transfer coefficient and Darcy friction coefficient, most of the experimental or computational studies of woven spacers presented up to now have considered only two orientations, with the main flow either parallel or orthogonal to the spacer filaments, or bisecting the angle formed by these latter.

Figure 9 (a, b) reports Nu and Sh (with different scales) as functions of the flow attack angle θ of a woven spacer-filled channel characterized by P/H=2 and Re_τ = 60 (i.e., for a given pressure drop per unit length). The corresponding Reynolds number ranges between ~160 and ~180 according to the value of θ. Graph (a) is for the interval θ=0-45°, while graph (b) is for the full interval θ=0-360°. As remarked above, for symmetry reasons this latter can be obtained by that for θ=0-45° by applying reflections and translations. In the interval 0–45°, there is a monotonic increase of mass transfer and a general increase of heat transfer, with only a small *plateau* around θ=15-20°.

Similarly, **Figure 9** (c, d) shows the angular dependence of the bulk Reynolds number Re and the Darcy friction coefficient normalized by that for a void plane channel, $f/(96/\mathrm{Re})$. Note the use of two separate scales. In the interval 0–45°, a non-monotonic behavior is observed for both quantities. The normalized friction coefficient exhibits a maximum for $\theta \approx 7°$ and a minimum for $\theta = 45°$. An opposite behavior is observed for the Reynolds number. Thus, the orientation $\theta = 45°$ exhibits both the lowest friction coefficient and the highest heat and mass transfer coefficient, which makes it the most promising for practical applications.

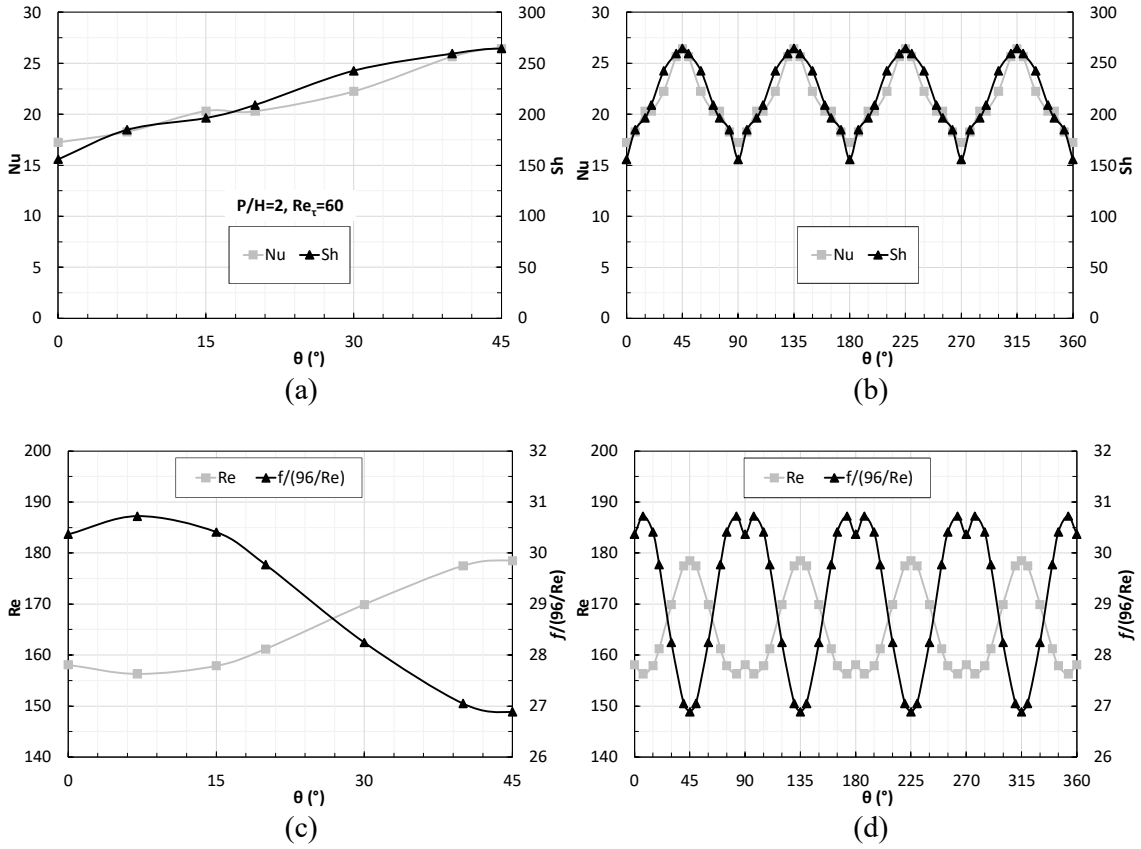

Figure 9. Influence of the flow attack angle on a,b) the Nusselt and Sherwood numbers and c,d) the bulk Reynolds number and the normalized friction coefficient $f/(96/\mathrm{Re})$ for a woven spacer filled channel characterized by $P/H=2$, $\mathrm{Re}_\tau=60$.

A similar behavior, characterized by higher Nusselt and Sherwood numbers and lower friction coefficients being attained for $\theta = 45°$ than for $\theta = 0°$, was obtained for all values of P/H investigated

at sufficiently low Reynolds numbers. Above a certain value of Re, depending on P/H, the effect of the flow attack angle on f remained similar, but the effect on Nu and Sh became small and, in some cases, opposite to that observed at lower Re.

3.4 Effect of P/H and Re

In regard to the influence of the Reynold number on pressure drop, **Figure 10** reports computational results for the Darcy friction coefficient f as a function of Re for two values of the flow attack angle θ (0, graph (a), and 45°, graph (b)) and three values of P/H (2, 3 and 4). For comparison purposes, results of non-woven spacers are reported as well. The presence of a spacer makes the friction coefficient increase with respect to a void (spacerless) channel, and the effect is larger for smaller values of the pitch to height ratio, i.e. smaller values of the channel's porosity. For Re less than ~10, f follows strictly a power law of slope −1 as in void channels, and the influence of the flow attack angle is negligible. For larger Re, f deviates from the strict Re^{-1} behavior and becomes larger for θ=0° than for θ=45°. The difference increases with Re and depends non-monotonically on P/H; at Re=2000, it is approximatively 20-30%. Non-woven spacers exhibit lower pressure drops, the f values being roughly halved with respect to those predicted for woven spacers. Higher differences occur at Re>400 for a flow attack angle θ=45°. A peculiarity of non-woven spacers at θ=0° is a transitional behaviour starting at Re>~700-1300.

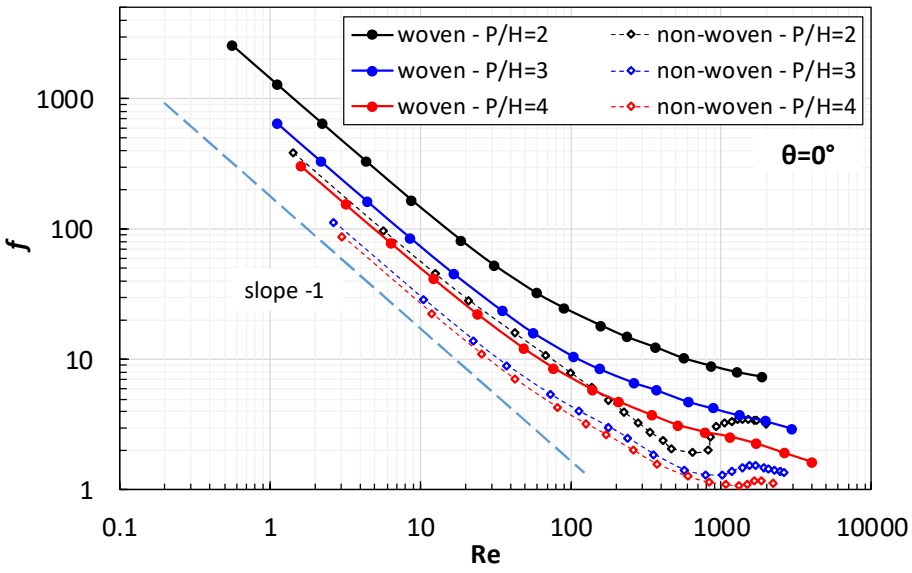

(a)

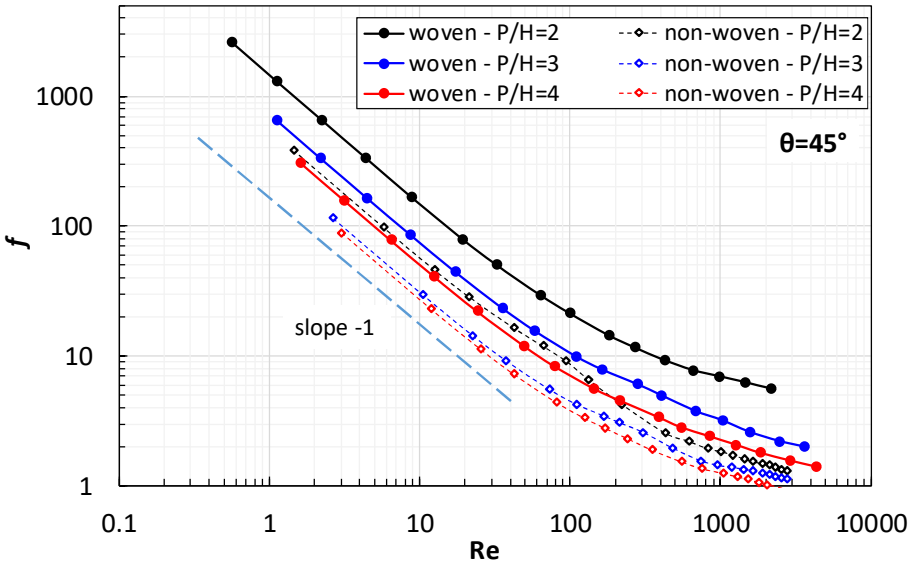

(b)

Figure 10. Darcy friction coefficient for woven spacers with $P/H = 2$, 3, and 4 as a function of the Reynolds number in log–log scale. (a) flow attack angle $\theta = 0°$; (b) flow attack angle $\theta = 45°$. Values of f computed for non-woven (overlapped) spacers of the same P/H and θ are reported for comparison purposes.

In regard to the influence of Reynolds number and pitch to height ratio on heat/mass transfer, **Figure 11** and **Figure 12** report the Nusselt and Sherwood numbers, respectively, as functions of Re for P/H=2, 3 or 4 and θ=0, graph (a), or 45°, graph (b). Again, results for non-woven spacers are reported for comparison.

The behavior of Nu with the Reynolds number, **Figure 11**, is characterized by a double asymptote. For very low Re (< 10, say) Nu approaches the flat behavior typical of creeping flows, with values between ~6 and ~7, little affected by P/H and θ. On the other hand, for Re>400-500, corresponding to turbulent flow, Nu approaches a linearly increasing trend, i.e. a power law of exponent 1. In the range Re=10-400 Nu increases at an intermediate rate. The influence of P/H and θ is largest in the median range Re=10-400, where the largest values of Nu are provided by spacers with P/H=2, θ=45°. Overall, the flow attack angle θ=45° leads to Nu values higher than those predicted for θ=0°. Moreover, the lower the P/H ratio, the higher the Nusselt number. Compared to the corresponding non-woven spacers (i.e. same P/H and θ), woven spacers provide higher Nu values in the whole range of Re investigated, with larger enhancement for intermediate values of Re. Interestingly, non-woven spacers exhibit a different and more complex effect of P/H and a lower effect of θ.

The behavior of Sh as a function of Re, **Figure 12**, is considerably different. At the lower end of the Reynolds number range, even for Re as low as 1 no clear asymptotic trend is observed, but rather a slow increase of Sh with Re, together with a marked dependence of Sh upon P/H and θ. At the upper end of the Re range, Sh increases approximately linearly with Re and attains very high values (~400) for the highest Re investigated (~300). As anticipated above, only steady laminar predictions are reported for Sh due to the difficulty of resolving the thin diffusive sublayer and to the unreliability of a "wall function" approach in such a complex recirculating flow.

The influence of P/H and θ on Sh is similar to that observed for the Nusselt number. Lower values of P/H lead to higher values of the Sherwood number, and the flow attack angle θ=45° enhances mixing compared to θ=0°. For any Re, highest values of Sh are provided, as for Nu, by the configuration P/H=2, θ=45°. In comparison with non-woven spacers, woven spacers yield higher mass transfer coefficients, especially at intermediate values of Re. Comparable values of Sh can be observed only for low Re and θ=0°.

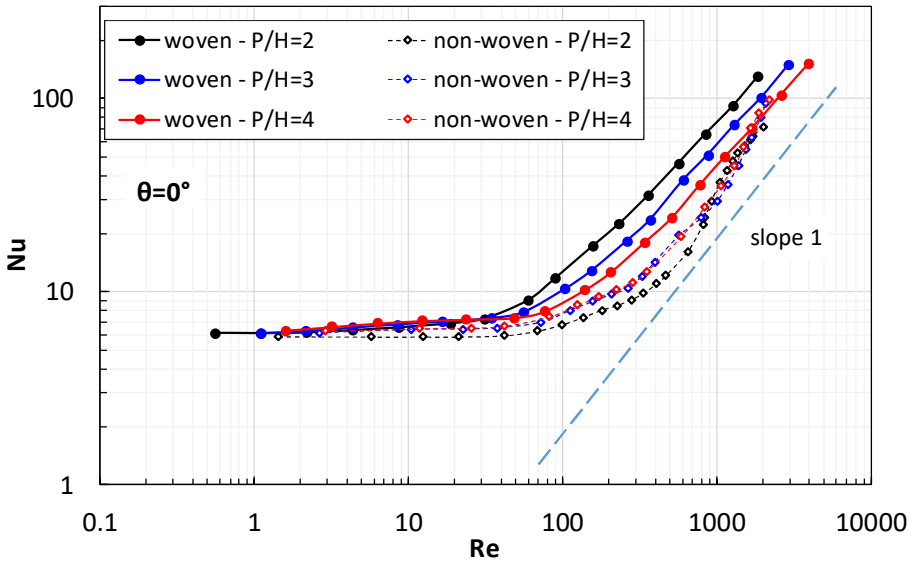

(a)

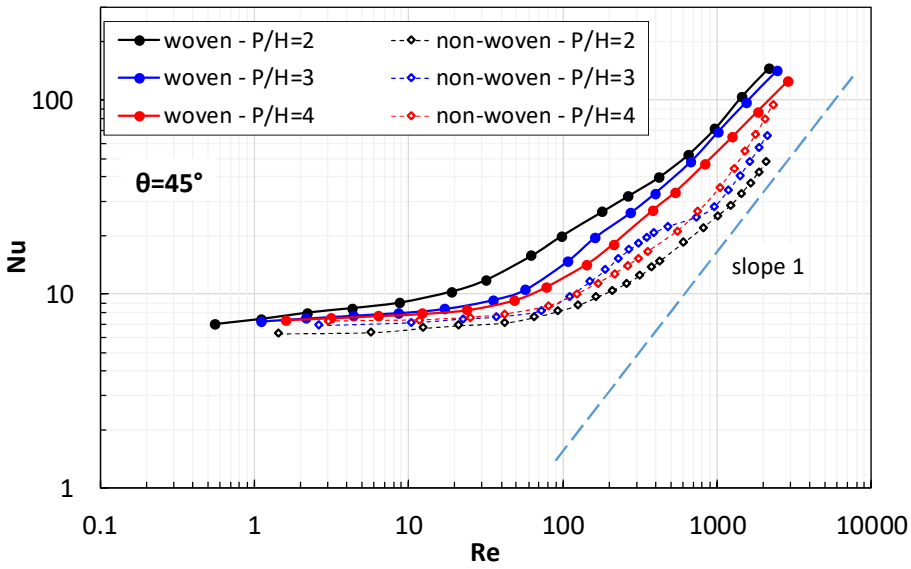

(b)

Figure 11. Nusselt number for woven spacers with P/H = 2, 3, and 4 as a function of the Reynolds number in log–log scale. (a) flow attack angle $\theta = 0°$; (b) flow attack angle $\theta = 45°$. Values of Nu computed for non-woven (overlapped) spacers of the same P/H and θ are reported for comparison purposes.

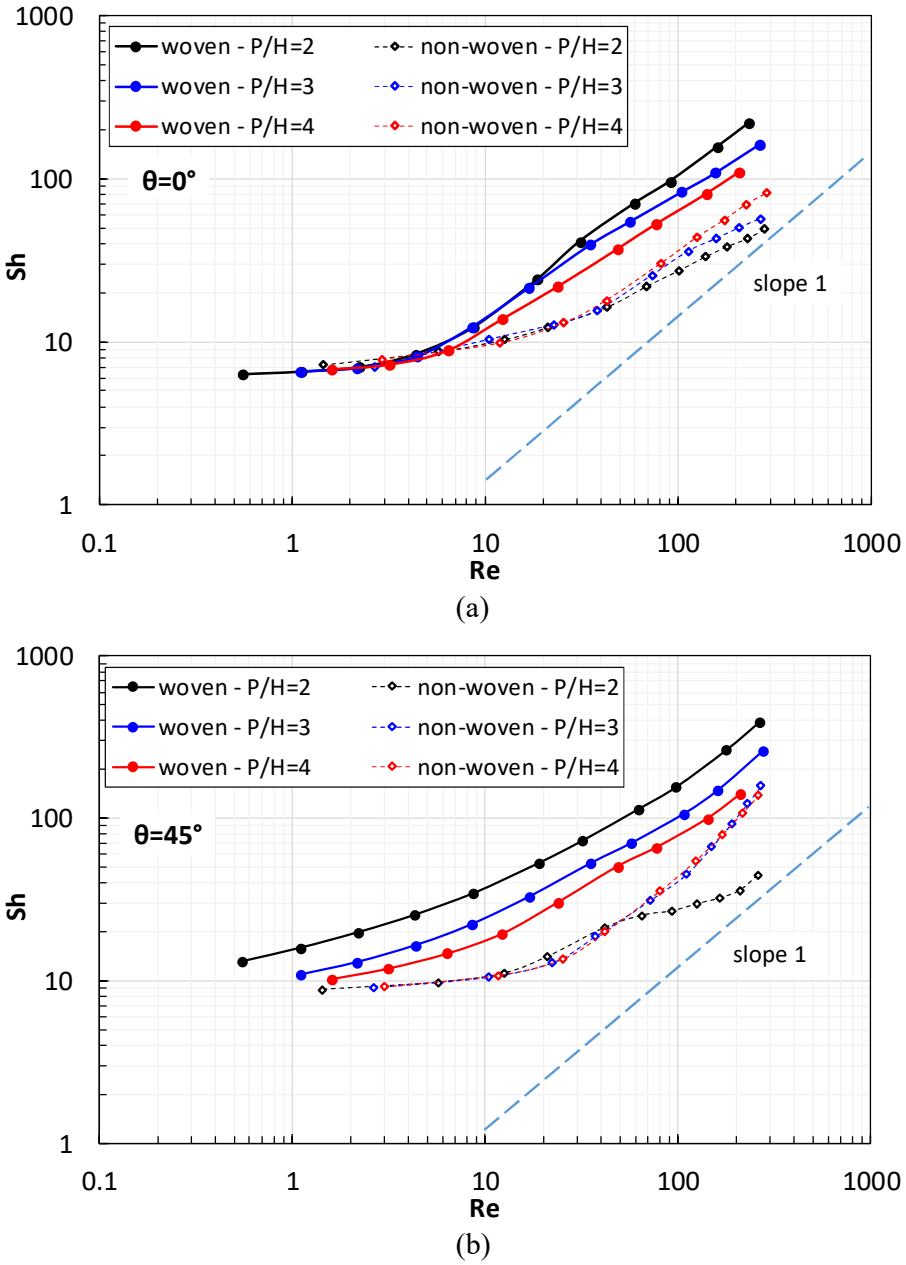

Figure 12. Sherwood number for woven spacers with $P/H = 2$, 3, and 4 as a function of the Reynolds number in log–log scale. (a) flow attack angle $\theta = 0°$; (b) flow attack angle $\theta = 45°$. Values of Sh computed for non-woven (overlapped) spacers of the same P/H and θ are reported for comparison purposes. The Schmidt number was 600 in all cases. Simulations were limited to laminar flow conditions.

3.5 Local distributions of Nusselt number and Sherwood number

In **Figures 13 and 14** the distributions of the local Nusselt and Sherwood numbers Nu_{loc}, Sh_{loc} on the top wall for the case θ=45° and different Reynolds numbers are reported for two values of P/H (2 and 4, respectively). Nu_{loc} and Sh_{loc} are normalized by their average values Nu and Sh, respectively. The same color scale is used in all Nu maps and in all Sh maps in order to make comparisons easier. The inset in each figure shows the relative arrangement of the wall considered in the maps with respect to the crossing woven filaments; the arrow indicates the main flow direction.

For each configuration, the location of minima and maxima of Nu_{loc}/Nu and Sh_{loc}/Sh are roughly the same; high-Nu_{loc} or Sh_{loc} spots correspond to regions where the fluid is pushed towards the wall by the shape of the filaments, low-Nu_{loc} or Sh_{loc} spots to regions where the fluid moves away from the wall. Absolute Nu_{loc} or Sh_{loc} minima correspond to the contact areas between filaments and wall. For both values of P/H, as Re increases the location of highly active and poorly active regions remains about the same, but the peaking factor of the distribution (ratio of maximum to minimum Nu_{loc} or Sh_{loc}) increases. For each quantity (Nu_{loc} or Sh_{loc}) and Reynolds number, as the pitch to height ratio P/H increases the relative importance of very high or very low Nu_{loc} or Sh_{loc} regions decreases while the central, diamond-shaped, area of intermediate and relatively flat Nu_{loc} or Sh_{loc} increases. Overall, the maps exhibit a high complexity, and the Sherwood number is distributed with a larger peaking factor than the Nusselt number. Note that some parts of the maps located in correspondence of the grid with tetrahedra are characterized by some graininess.

Figure 15 reports the distribution on a wall of the local Nusselt number (Nu_{loc}) for the case θ=0°, P/H=4, and Re_τ=60 by comparing results predicted by the SST turbulence model and the DNS, showing a good agreement.

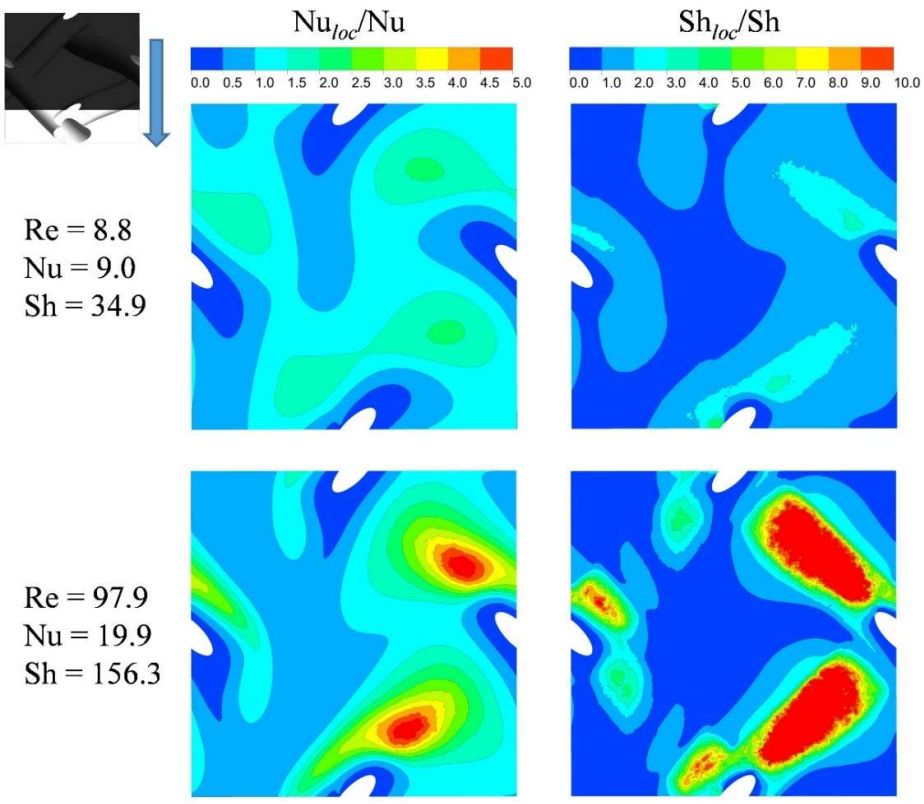

Figure 13. Maps of the normalized local Nusselt and Sherwood numbers on a wall for θ=45°, P/H=2 and two values of the Reynolds number. Average Nu and Sh values are also indicated.

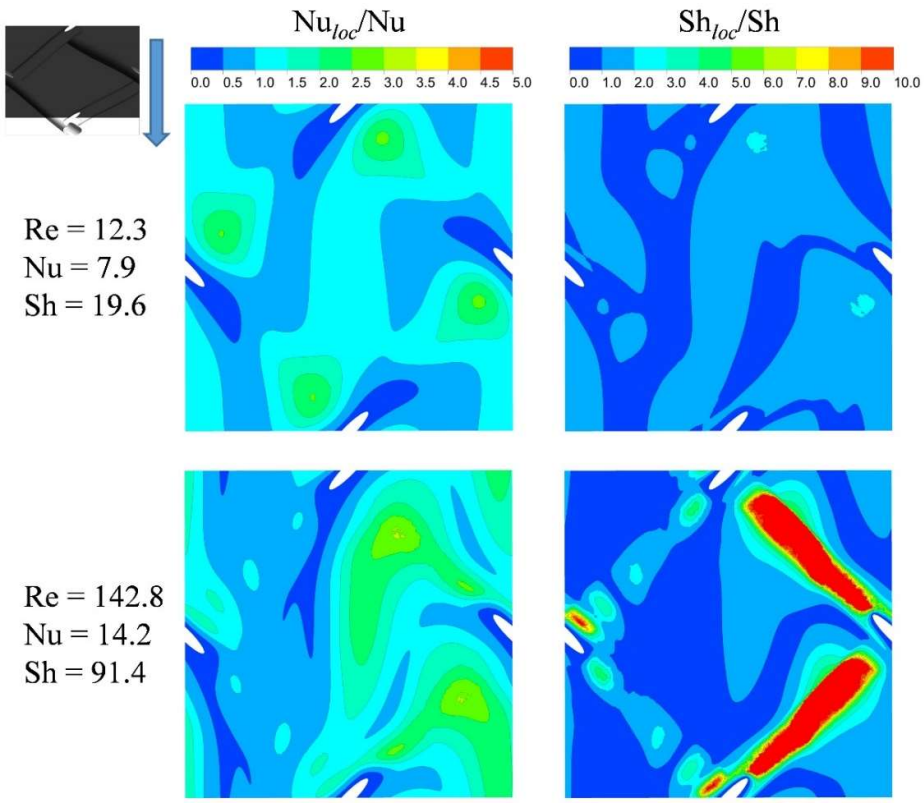

Figure 14. Maps of the normalized local Nusselt and Sherwood numbers on a wall for θ=45°, P/H=4 and two values of the Reynolds number. Average Nu and Sh values are also indicated.

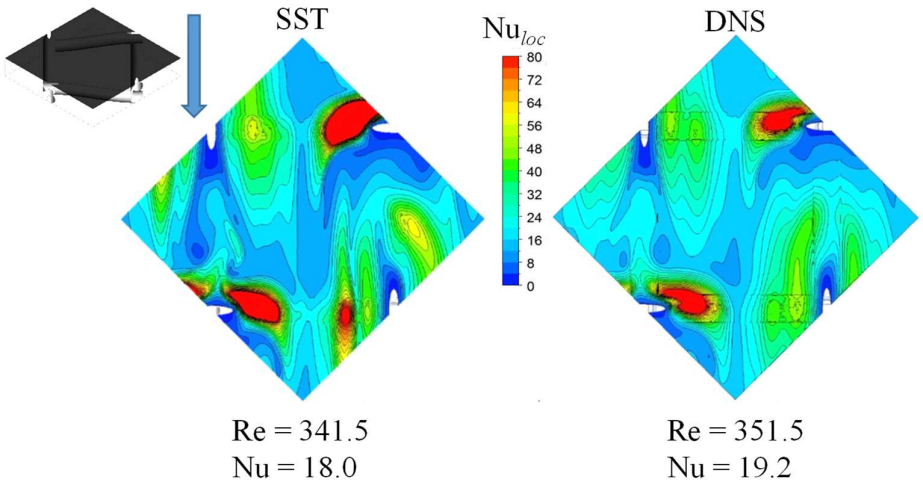

Figure 15. Maps of the local Nusselt number on a wall for θ=0°, P/H=4 and frictional Reynolds number of 60 predicted by the SST turbulence model and the DNS. Reynolds numbers and average Nu values are also indicated.

4. Conclusions

In the present paper, flow and heat/mass transfer characteristics (*f*, Nu, Sh) were predicted by computational fluid dynamics for channels provided with spacers consisting of two interwoven layers of mutually orthogonal cylindrical filaments. This work makes a further step towards a thorough characterization of woven spacer-filled channels, by investigating a broad range of flow attack angle (0-45°), pitch to height ratio *(P/H* =2, 3, 4) and Reynolds number (~1-4000). The results of the study can be summarized as follows.

- The dependence of *f*, Nu and Sh upon the Reynolds number cannot be described by a power-law in the whole range of Re simulated, but is approximately characterized by a double asymptotic trend. At the left end of the range (Re < 10, say) *f* follows strictly a 1/Re behavior while Nu is about constant, as in laminar parallel flow. The behavior of Sh resembles that of Nu for the 0°-orientation, while for θ=45° it exhibits a significant dependence on the Reynolds number even at Re as low as 1 or less. At the right end of the range investigated (Re>400, say) the friction coefficient approximately exhibits a $Re^{-1/2}$ dependence while Nu and Sh approach a linear trend, i.e. a power law of exponent one. In the intermediate range Re=10-400 all quantities exhibit an intermediate behaviour.
- The flow attack angle plays a significant role in determining flow and heat/mass transfer characteristics (Nu and Sh), while it has a lesser influence on pressure drop. For all Re and *P/H*, the best performance is obtained with the configuration θ=45°; the advantage of this configuration on other flow attack angles is largest in laminar flow (Re<~400) and decreases as Re increases and the flow becomes turbulent.
- The filament spacing has also a significant effect on flow and heat/mass transfer for all Re studied. In general, as *P/H* decreases both Nu and Sh increase, but the friction coefficient increases even more.

- A comparison with computational results regarding non-woven spacers shows that woven spacers are more effective for mixing enhancement, especially at intermediate values of the Reynolds number, but are characterized by a higher hydraulic friction.

Two further conclusive remarks are appropriate.

First, the optimum operating spacer configuration (P/H, θ) is necessarily a compromise between low friction and high heat / mass transfer rates; however, the relative weights to be attributed to the two performance parameters depend on the specific application and on the exact definition of the target to be achieved. For example, in Membrane Distillation a high heat transfer coefficient is much desirable because polarization losses are a large fraction of the overall driving force (temperature difference), while a low friction coefficient is less crucial because pumping losses are usually negligible. On the other hand, in Reverse Electrodialysis low pumping losses are crucial for the possibility itself of a positive net energy output, whereas a large mass transfer coefficient is only marginally beneficial because concentration polarization losses are but a small fraction of the applied driving force (electric potential difference). Synthetic merit figures, often proposed in the form Nu^a/f^b or Sh^a/f^b (with a and b suitable exponents), may be of some use, but the only rigorous approach to optimization is the minimization of a well defined cost function, in which both pressure losses and heat / mass transfer rates explicitly appear. Such study is beyond the scope of the present study, but efforts in this direction have been proposed by some of the present authors for specific applications [33,34].

Second, in plant design and optimization one would be able to predict performance parameters f and Nu or Sh for arbitrary values of the operating parameters (Re, P/H and θ) in a suitably broad range. Now, even in the presence of a significant body of experimental results concerning friction and heat / mass transfer in spacer-filled channels, translating these data into practical correlations is a non-trivial task. In fact, the complexity and non-monotonicity of the relevant functional dependence and the heavy interaction between the various parameters rule out a separate-variable treatment and the use of power-law correlations. The best approach to any optimization study is probably the

availability of a sufficiently large database of Nu/Sh numbers and friction coefficients, among which to interpolate. In this direction, CFD can represent a unique “smart interpolation” tool which can lead from a sparse set of experimental data to a dense matrix of validated predictions.

Nomenclature

Symbol	Quantity	Unit
$\tilde{c}$	Periodic component of concentration	mol m^{-3}
c_b	Bulk concentration	mol m^{-3}
c_p	Specific heat capacity	J kg^{-1} K^{-1}
c_w	Wall concentration	mol m^{-3}
D	Salt diffusivity	m^2 s^{-1}
d	Spacer wires diameter	m
$d_{h,void}$	Hydraulic diameter of the void channel	m
f	Darcy friction coefficient	
H	Channel height	m
J''_w	Molar flux at the wall	mol m^{-2} s^{-1}
K_c	Variation of bulk concentration per unit length	mol m^{-4}
K_p	Pressure loss per unit length	Pa m^{-1}
K_T	Variation of energy per unit length	J m^{-4}
Nu	Nusselt number	
Nu_{loc}	Local Nusselt number	
P	Filaments pitch	m
Pr	Prandtl number	
Pn	Power number	
p	Pressure	Pa
$\tilde{p}$	Periodic component of pressure	Pa
q''_w	Heat flux at the wall	W m^{-2}
Re	Bulk Reynolds number	
Re_τ	Frictional Reynolds number	
Sc	Schmidt number	
Sh	Sherwood number	
Sh_{loc}	Local Sherwood number	
s	Coordinate along the main flow direction	m
s_i	i-th component of the unit vector **s** directed along the main flow direction	m
$\tilde{T}$	Periodic component of temperature	K
T_b	Bulk temperature	K
T_w	Wall temperature	K
U_{void}	Mean velocity in the void channel	m s^{-1}

U_τ	Friction velocity	m s^{-1}
u_i	*i*-th velocity component	m s^{-1}
u_s	Local velocity component along the main flow direction	m s^{-1}
x_i	*i*-th coordinate	m

Greek symbols

θ	Flow attack angle	deg
λ	Thermal conductivity	W m^{-1} K^{-1}
μ	Dynamic viscosity	kg m^{-1} s^{-1}
ν	Kinematic viscosity	m^2 s^{-1}
ρ	Density	kg m^{-3}

Averages

$\langle \quad \rangle$	Over the wall (fluid-membrane interface)

References

[1] W. Li, X. Su, A. Palazzolo, S. Ahmed, Numerical modeling of concentration polarization and inorganic fouling growth in the pressure-driven membrane filtration process, J. Memb. Sci. 569 (2019) 71–82. doi:10.1016/j.memsci.2018.10.007.

[2] K.Y. Toh, Y.Y. Liang, W.J. Lau, G.A. Fimbres Weihs, A review of CFD modelling and performance metrics for osmotic membrane processes, Membranes (Basel). 10 (2020) 1–30. doi:10.3390/membranes10100285.

[3] S. Kerdi, A. Qamar, A. Alpatova, J.S. Vrouwenvelder, N. Ghaffour, Membrane filtration performance enhancement and biofouling mitigation using symmetric spacers with helical filaments, Desalination. 484 (2020) 114454. doi:10.1016/j.desal.2020.114454.

[4] N. Sreedhar, N. Thomas, O. Al-Ketan, R. Rowshan, H.H. Hernandez, R.K. Abu Al-Rub, H.A. Arafat, Mass transfer analysis of ultrafiltration using spacers based on triply periodic minimal surfaces: Effects of spacer design, directionality and voidage, J. Memb. Sci. 561 (2018) 89–98. doi:10.1016/j.memsci.2018.05.028.

[5] A. Anvari, A. Azimi Yancheshme, K.M. Kekre, A. Ronen, State-of-the-art methods for overcoming temperature polarization in membrane distillation process: A review, J. Memb. Sci. 616 (2020) 118413. doi:10.1016/j.memsci.2020.118413.

[6] J. Phattaranawik, R. Jiraratananon, A.G. Fane, C. Halim, Mass flux enhancement using spacer filled channels in direct contact membrane distillation, J. Memb. Sci. 187 (2001) 193–201. doi:10.1016/S0376-7388(01)00344-1.

[7] A.E. Anqi, M. Usta, R. Krysko, J.-G. Lee, N. Ghaffour, A. Oztekin, Numerical study of desalination by vacuum membrane distillation – Transient three-dimensional analysis, J. Memb. Sci. (2019) 117609. doi:10.1016/j.memsci.2019.117609.

[8] L. Gurreri, A. Tamburini, A. Cipollina, G. Micale, M. Ciofalo, Flow and mass transfer in spacer-filled channels for reverse electrodialysis: a CFD parametrical study, J. Memb. Sci. 497 (2016) 300–317. doi:10.1016/j.memsci.2015.09.006.

[9] F. Li, W. Meindersma, A.B. De Haan, T. Reith, Experimental validation of CFD mass transfer simulations in flat channels with non-woven net spacers, J. Memb. Sci. 232 (2004) 19–30. doi:10.1016/j.memsci.2003.11.015.

[10] J. Liu, A. Iranshahi, Y. Lou, G. Lipscomb, Static mixing spacers for spiral wound modules, J. Memb. Sci. 442 (2013) 140–148. doi:10.1016/j.memsci.2013.03.063.

[11] A. Hagedorn, G. Fieg, D. Winter, J. Koschikowski, A. Grabowski, T. Mann, Membrane and spacer evaluation with respect to future module design in membrane distillation, Desalination. 413 (2017) 154–167. doi:10.1016/j.desal.2017.03.016.

[12] R.D. Gustafson, J.R. Murphy, A. Achilli, A stepwise model of direct contact membrane distillation for application to large-scale systems: Experimental results and model predictions, Desalination. 378 (2016) 14–27. doi:10.1016/j.desal.2015.09.022.

[13] A.P. Straub, N.Y. Yip, M. Elimelech, Raising the Bar: Increased Hydraulic Pressure Allows Unprecedented High Power Densities in Pressure-Retarded Osmosis, Environ. Sci. Technol. Lett. 1 (2013) 55–59. doi:10.1021/ez400117d.

[14] L. Gurreri, A. Tamburini, A. Cipollina, G. Micale, M. Ciofalo, Pressure drop at low Reynolds numbers in woven-spacer-filled channels for membrane processes: CFD prediction and experimental validation, Desalin. Water Treat. 61 (2017) 170–182. doi:10.5004/dwt.2016.11279.

[15] F.N. Ponzio, A. Tamburini, A. Cipollina, G. Micale, M. Ciofalo, Experimental and computational investigation of heat transfer in channels filled by woven spacers, Int. J. Heat Mass Transf. 104 (2017) 163–177. doi:10.1016/j.ijheatmasstransfer.2016.08.023.

[16] L. Gurreri, A. Tamburini, A. Cipollina, G. Micale, M. Ciofalo, CFD prediction of concentration polarization phenomena in spacer-filled channels for reverse electrodialysis, J. Memb. Sci. 468 (2014) 133–148. doi:10.1016/j.memsci.2014.05.058.

[17] M. Ciofalo, F. Ponzio, A. Tamburini, A. Cipollina, G. Micale, Unsteadiness and transition to turbulence in woven spacer filled channels for Membrane Distillation, J. Phys. Conf. Ser. 796 (2017) 012003. doi:10.1088/1742-6596/796/1/012003.

[18] L. Gurreri, A. Tamburini, A. Cipollina, G. Micale, M. Ciofalo, Performance comparison between overlapped and woven spacers for membrane distillation, Desalin. Water Treat. 69 (2017) 178–189. doi:10.5004/dwt.2017.20236.

[19] M. Johannink, K. Masilamani, A. Mhamdi, S. Roller, W. Marquardt, Predictive pressure drop models for membrane channels with non-woven and woven spacers, Desalination. 376 (2015) 41–54. doi:10.1016/j.desal.2015.07.024.

[20] B. Gu, C.S. Adjiman, X.Y. Xu, The effect of feed spacer geometry on membrane performance and concentration polarisation based on 3D CFD simulations, J. Memb. Sci. 527 (2017) 78–91. doi:10.1016/j.memsci.2016.12.058.

[21] F. Dong, D. Jin, S. Xu, L. Xu, X. Wu, P. Wang, Q. Leng, R. Xi, Numerical simulation of flow and mass transfer in profiled membrane channels for reverse electrodialysis, Chem. Eng. Res. Des. 157 (2020) 77–91. doi:10.1016/j.cherd.2020.02.025.

[22] K.Y. Toh, Y.Y. Liang, W.J. Lau, G.A. Fimbres Weihs, 3D CFD study on hydrodynamics and mass transfer phenomena for SWM feed spacer with different floating characteristics, Chem. Eng. Res. Des. 159 (2020) 36–46. doi:10.1016/j.cherd.2020.04.010.

[23] M. La Cerva, A. Cipollina, M. Ciofalo, M. Albeirutty, N. Turkmen, S. Bouguecha, G. Micale, CFD Investigation of Spacer-Filled Channels for Membrane Distillation, Membranes (Basel). 9 (2019) 91. doi:10.3390/membranes9080091.

[24] G. Battaglia, L. Gurreri, G. Airò Farulla, A. Cipollina, A. Pirrotta, G. Micale, M. Ciofalo, Membrane Deformation and Its Effects on Flow and Mass Transfer in the Electromembrane Processes, Int. J. Mol. Sci. 20 (2019) 1840. doi:10.3390/IJMS20081840.

[25] D.C. Wilcox, Reassessment of the scale-determining equation for advanced turbulence models, AIAA J. 26 (1988) 1299–1310. doi:10.2514/3.10041.

[26] C.L.V. Jayatilleke, The influence of Prandtl number and surface roughness on the resistance of the laminar sub-layer to momentum and heat transfer, Prog. Heat Mass Transf. 1 (1969) 193–329.

[27] A. Tamburini, M. Renda, A. Cipollina, G. Micale, M. Ciofalo, Investigation of heat transfer in spacer-filled channels by experiments and direct numerical simulations, Int. J. Heat Mass Transf. 93 (2016) 1190–1205. doi:10.1016/j.ijheatmasstransfer.2015.11.034.

[28] M. La Cerva, M. Ciofalo, L. Gurreri, A. Tamburini, A. Cipollina, G. Micale, On some issues in the computational modelling of spacer-filled channels for membrane distillation, Desalination. 411 (2017) 101–111. doi:10.1016/j.desal.2017.02.016.

[29] L. Francis, N. Ghaffour, A.S. Alsaadi, S.P. Nunes, G.L. Amy, Performance evaluation of the DCMD desalination process under bench scale and large scale module operating conditions, J. Memb. Sci. 455 (2014) 103–112. doi:10.1016/j.memsci.2013.12.033.

[30] D. Winter, J. Koschikowski, M. Wieghaus, Desalination using membrane distillation: Experimental studies on full scale spiral wound modules, J. Memb. Sci. 375 (2011) 104–112. doi:10.1016/j.memsci.2011.03.030.

[31] M. Ciofalo, M. La Cerva, M. Di Liberto, A. Tamburini, Influence of the boundary conditions on heat and mass transfer in spacer-filled channels, J. Phys. Conf. Ser. 923 (2017) 012053. doi:10.1088/1742-6596/923/1/012053.

[32] M. Ciofalo, F. Cacciatore, M. Di Liberto, A. Tamburini, Experimental investigation of two-side heat transfer in spacer-filled channels, in: J. Phys. Conf. Ser., IOP Publishing Ltd, 2020: p. 012005. doi:10.1088/1742-6596/1599/1/012005.

[33] M. Ciofalo, M. La Cerva, M. Di Liberto, L. Gurreri, A. Cipollina, G. Micale, Optimization of net power density in Reverse Electrodialysis, Energy. 181 (2019) 576–588. doi:10.1016/j.energy.2019.05.183.

[34] M. La Cerva, L. Gurreri, A. Cipollina, A. Tamburini, M. Ciofalo, G. Micale, Modelling and cost analysis of hybrid systems for seawater desalination: Electromembrane pre-treatments for Reverse Osmosis, Desalination. 467 (2019) 175–195. doi:10.1016/j.desal.2019.06.010.